Drivers for seasonal variability in sea level around the China seas

Ying Qu [a,b,c], Svetlana Jevrejeva [b,d], Joanne Williams [b], John C. Moore [a,e,f,*]

[a] College of Global Change and Earth System Science, Beijing Normal University, Beijing, China
[b] National Oceanography Centre, 6 Brownlow Street, Liverpool, L3 5DA, UK
[c] State Key Laboratory of Cryospheric Science, Northwest Institute of Eco-Environment and Resources, Chinese Academy of Sciences, Lanzhou 730000, China
[d] Centre for Climate Research Singapore, Meteorological Service Singapore, Singapore
[e] Arctic Centre, University of Lapland, P.O. Box 122, 96101 Rovaniemi, Finland
[f] CAS Center for Excellence in Tibetan Plateau Earth Sciences, Beijing 100101, China

ABSTRACT

Globally variable ocean and atmospheric dynamics lead to spatially complex seasonal cycles in sea level. The China Seas, that is the Bohai, Yellow, East China and the South China seas, is a region with strong seasonal amplitudes, and straddles the transition between tropical and temperature zones, monsoonal and westerlies, shelf and deep ocean zones. Here we investigate the drivers for seasonal variability in sea level from tide gauge records, satellite altimetry along with output from the NEMO (Nucleus for European Modeling of the Ocean) model including sea surface height and ocean bottom pressure along with meteorological data in the China Seas. The seasonal cycle accounts for 37% - 94% of monthly sea level variability in 81 tide gauge records, ranging from 18 to 59 cm. We divided the seasonal cycles into four types: 1) an asymmetric sinusoid; 2) a clearly defined peak on a flat background; 3) a relatively flat signal; 4) a symmetric co-sinusoid. Type 1 is found in northern China and Taiwan, Korea, Japan and The Philippines where Inverse Barometer (IB) effects dominates seasonality along with a steric contribution. The seasonal monsoon associated with barotropic response and freshwater exchange play important roles in type 2, (eastern and southern Chinese coasts), type 3 (East Malaysia) and type 4 (Vietnam and Gulf of Thailand). IB corrected seasonal cycle amplitudes are larger in continental shelf areas than the deep ocean, with a maximum in the Gulf of Thailand, and NEMO underestimates the seasonal amplitude along the coast by nearly 50%.

1. Introduction

The severity of coastal flooding often depends on the phases of large amplitude seasonal cycles in local sea level (Wahl et al., 2014; Amiruddin et al., 2015). Accurate future coastal sea level projections require detailed understanding of seasonal variability (Qu et al., 2019). Seasonal differences in sea level at individual locations are up to 0.6 m, which is larger than projected sea level rise by 2070 under the IPCC RCP8.5 scenario (Jevrejeva et al., 2019; Qu et al., 2019). Thus, understanding and being able to model seasonal sea level variability will greatly aid coastal communities in being prepared for extreme coastal flooding events and therefore inform strategies to mitigate the associated impacts (Feng et al., 2015).

Significant efforts have been made to elucidate the drivers and mechanisms contributing to seasonal sea level variability (Menendez et al., 2009; Dangendorf et al., 2012; Wahl et al., 2014; Amiruddin et al.,

2015; Feng et al., 2015). Seasonal sea level variability may be driven by a variety of mechanisms including: atmospheric pressure and winds; precipitation; river runoff; seasonal ice melting; ocean circulation changes; and variations in steric height from changes in sea level driven by expansion or contraction of the water column above the seasonal thermocline in response to heat flux and water exchange with the atmosphere (Gill and Niiler, 1973; Tsimplis and Woodworth, 1994). Glacio-isostatic forcing contributes little to the seasonal variability (Pugh and Woodworth, 2014) and hence is neglected in this study.

The forcing factors driving sea level vary between regions (Dangendorf et al., 2012; Amiruddin et al., 2015; Feng et al., 2015). Tide gauge records from Cuxhaven in the North Sea show that on seasonal timescales, the variability is due mainly to wind stresses; sea level pressure and precipitation are smaller but also significant factors (Dangendorf et al., 2012, 2013). In the South China Sea, monsoon season winds are the main drivers of seasonal sea level variability along the

Gulf of Thailand (Saramul and Ezer, 2014; Amiruddin et al., 2015). In the deeper parts of the South China Sea, the steric component of sea level dominates variability whereas the mass component is dominant in the shallow waters (Cheng and Qi, 2010), while in the open ocean especially eddy-rich regions, the monthly sea level is mainly driven by mesoscale eddies (Feng et al., 2015).

High-resolution NEMO model simulations along with satellite altimetry provide global coverage of sea level observations which can be used to explore the seasonal sea level variability. Fig.1 shows the annual amplitude and phase globally from satellite altimetry and the NEMO model for the period 1993–2012. The largest amplitudes are associated with western boundary currents such as in the Kuroshio and Gulf Stream regions, and within the tropical Pacific and Indian Oceans (Vinogradov et al., 2008), but also along shallow semi-enclosed, and coastal areas, including the China Seas. China itself has 32 thousand kilometres of coastline including 18 thousand kilometres of mainland and 14 thousand kilometres of island coast. Many large cities are located along the

coast both in China and neighboring countries, with ever-increasing populations and economically important infrastructure (Jevrejeva et al., 2016; Abadie et al., 2020). There are also globally significant coastal wetlands and ecosystems that are particularly sensitive to sea level rise (Woodruff et al., 2013). High amplitude seasonality makes it, and neighboring countries vulnerable to sea level rise. Thus, it is societally relevant to determine the drivers of this seasonal variability in sea level around the China Seas and how they relate to the complex oceanographical and meteorological conditions.

Previous studies of the seasonal sea level cycle on a regional or global scale are usually based on tide gauge records or satellite altimetry. The former is sparsely distributed and though the latter provides a near global coverage, it only covers a relatively short period. NEMO model outputs provide high resolution simulation of sea surface height and ocean bottom pressure at global scale since the 1950s, allowing extended spatial resolution and temporal assessment. In this study, we analyze the seasonal sea level cycle around the China Seas using
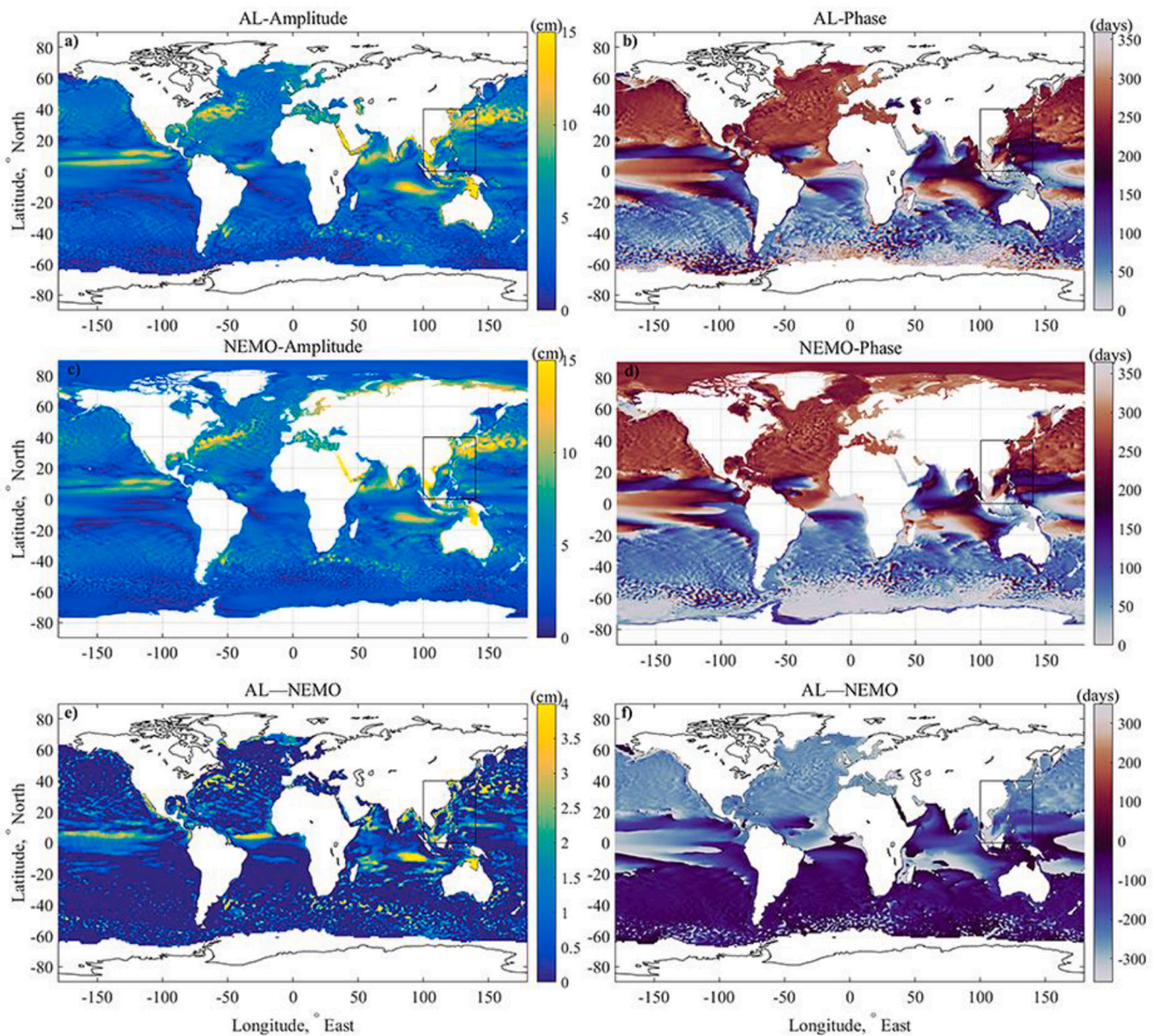

Fig. 1. Global annual amplitude of the sea level from a) satellite altimetry (AL), c) NEMO model outputs (NEMO), and e) satellite altimetry minus NEMO; and global annual phase of the sea level from b) satellite altimetry, d) NEMO model outputs, and f) satellite altimetry minus NEMO from 1993 to 2012. Phases are expressed in days, and zero phase is the middle of January. The study area is marked by black rectangles.

observational datasets including tide gauge records, satellite altimetry, reanalysis datasets, observational temperature and salinity data. We divide the seasonal cycles of all tide gauge records around the China Seas into different types according to their characteristics of seasonal cycles, geography and associated drivers of seasonal sea level variability. We quantitatively explore results from NEMO model simulations of sea surface height to differences in sea surface height offshore and in the deep ocean. The assimilation of observational datasets and model simulations analyzed with some novel methods allows elucidation of the seasonal variability in the globally important and sensitive China Seas region.

2. Data

In this analysis, several datasets from different sources were used. We used monthly tide gauge records from 81 locations obtained from the Permanent Services for Mean Sea level (PSMSL) (Holgate et al., 2013; Permanent Service for Mean Sea level (PSMSL), 2017). The 81 stations are shown in Fig.2 and their record durations in Fig.3. North Point and Quarry Bay in Hong Kong have identical locations (Ding et al., 2001), so we merged them into one time series and rename it as NPQB.

Climatic and meteorological factors were characterized by monthly mean sea level pressure, monthly surface zonal (u) and meridional (v) winds at the 10 m level from NCEP/NCAR Reanalysis datasets (https ://psl.noaa.gov/data/gridded/data.ncep.reanalysis.-derived.surfacef lux.html; Kalnay et al., 1996; Compo et al., 2011).

We utilized high-resolution (0.25° × 0.25°) monthly satellite altimetry data spanning 1993 to 2016 from AVISO (Archiving, Validation, and Interpretation of Satellite Oceanographic Data). The dataset is a merged product consists of monthly averaged sea level anomalies from multi-mission gridded sea surface height anomalies including T/P, Jason-1&2, Envisat, ERS-1&2, Cryosat-2 et al. Standard corrections for oceanic and atmospheric dynamics have been made including the ocean tide, the pole tide, the ionospheric correction, the dry and wet tropospheric correction, and the dynamic atmospheric correction (Carrère and Lyard, 2003; Feng et al., 2015).

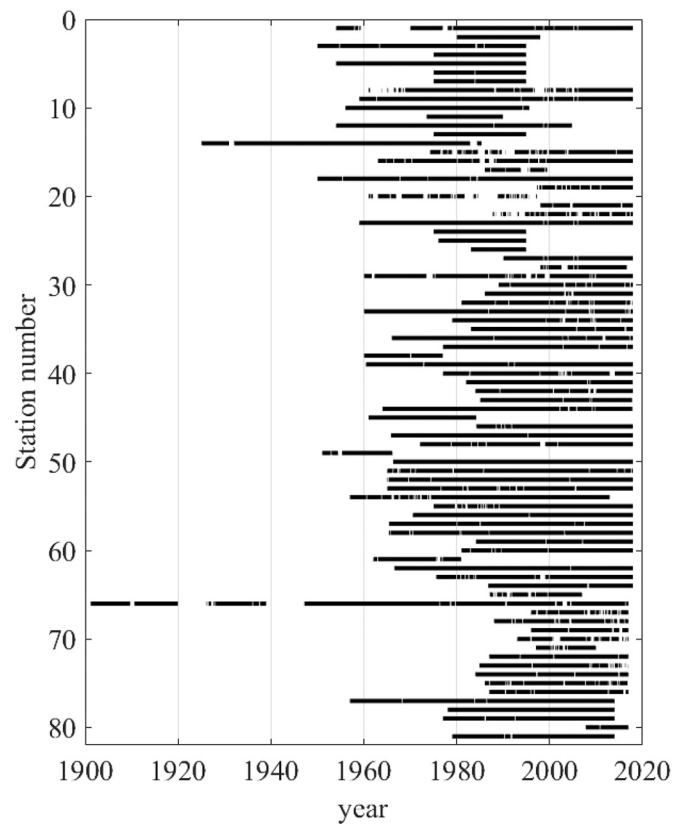We used EN4.2.0 quality-controlled monthly ocean temperature and

Fig. 3. The time spanned by each tide gauge record.

salinity datasets (Good et al., 2013), in which biases from mechanical bathythermograph and expendable bathythermograph profiles were corrected following Gouretski and Reseghetti (2010).

High-resolution (1/12° × 1/12°) NEMO (Marsh et al., 2009) simulations of sea surface height from the N006 run at the National Oceanography Centre, on the ORCA 1/12° tripolar grid (Hughes et al., 2018) were used to study seasonal variability. The Drakkar Surface Forcing data set was used for surface air temperature, surface radiative heat fluxes, humidity, winds and precipitation to force the model (Brodeau et al., 2010; Dussin et al., 2014). Tides are not taken in to account. More details can be found in Moat et al. (2016) and Hughes et al. (2018). No atmospheric pressure forcing was included in the simulation, so the simulated sea surface height can be regarded as inverse barometer-corrected dynamic topography. The NEMO model simulations covered the period 1959–2012, the simulation output is 5-day averages starting at the beginning of every year, and we calculate monthly mean sea surface height to define seasonal cycles.

3. Methods

To estimate the harmonic parameters of the annual and semi-annual sea level cycles, we removed the linear trend and the mean of times series and then estimated annual and semi-annual harmonics following Amiruddin et al. (2015) using a least squares fit to the residual monthly sea level M:

$$M = A_a cos\left(\frac{2\pi}{365.25}(t - P_a)\right) + A_{sa} cos\left(\frac{2\pi}{182.63}(t - P_{sa})\right) \quad (1)$$

where A and P refer to amplitude and phase of the harmonic and the subscripts a and sa refer to annual and semi-annual components, and t is time in sidereal days which is running in the sequence 15, 45, 75, etc. Phases are expressed in days, and zero phase is the middle of January.

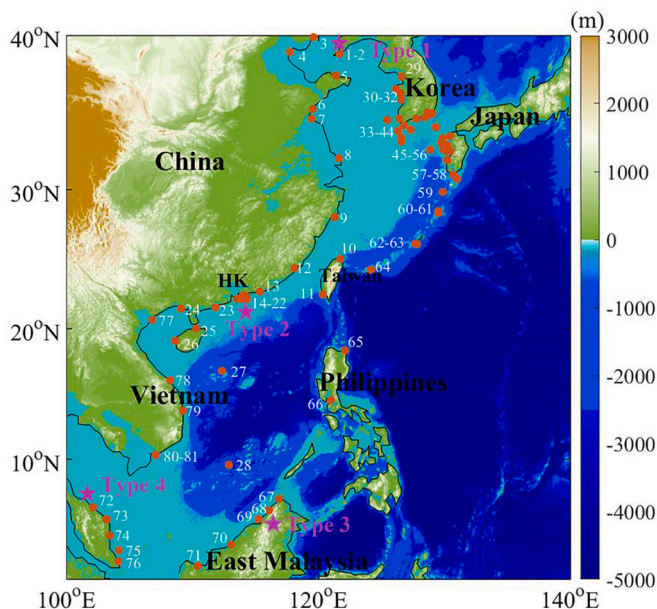The total sea level is the sum of three subcomponents: the barometric

Fig. 2. The bathymetry map of the study area showing the location of tide gauge stations around the China Seas (numbered, red points). The archetypal locations for Types 1 to 4 are shown by purple stars. (For interpretation of the references to colour in this figure legend, the reader is referred to the web version of this article.)

term, the steric term and the contribution from ocean bottom pressure:

$$\eta = \eta_a + \eta_{steric} + \eta_b \qquad (2)$$

η is the total sea level, η_a is the contribution from barometric effects to sea level, η_{steric} is the contribution from steric and η_b is the contribution from ocean bottom pressure.

The inverse-barometer effects can be corrected following:

$$\eta_a = -\frac{p_a}{g\rho_0} \qquad (3)$$

p_a is the atmospheric surface pressure, ρ_0 is the reference density (1025 kg/m^3) of sea water,

g is the acceleration of gravity.

Depth-integrated steric sea level (η_{steric}) was computed from the density profile over depth, z, which we derived from gridded potential temperature and salinity data following (Dangendorf et al., 2014):

$$\eta_{steric} = -\frac{1}{\rho_0} \int_{-H}^{0} (\rho - \overline{\rho}) dz \qquad (4)$$

Where ρ is in situ density computed from temperature (T) and salinity (S) observations with the TEOS-10 software (McDougall and Barker, 2011), $\overline{\rho}$ is the time averaged density over the whole record duration, and H is the basin depth below mean sea level.

The sea surface height (h) from NEMO is the sum of variations associated with ocean bottom pressure p_b and steric height (Φ). We
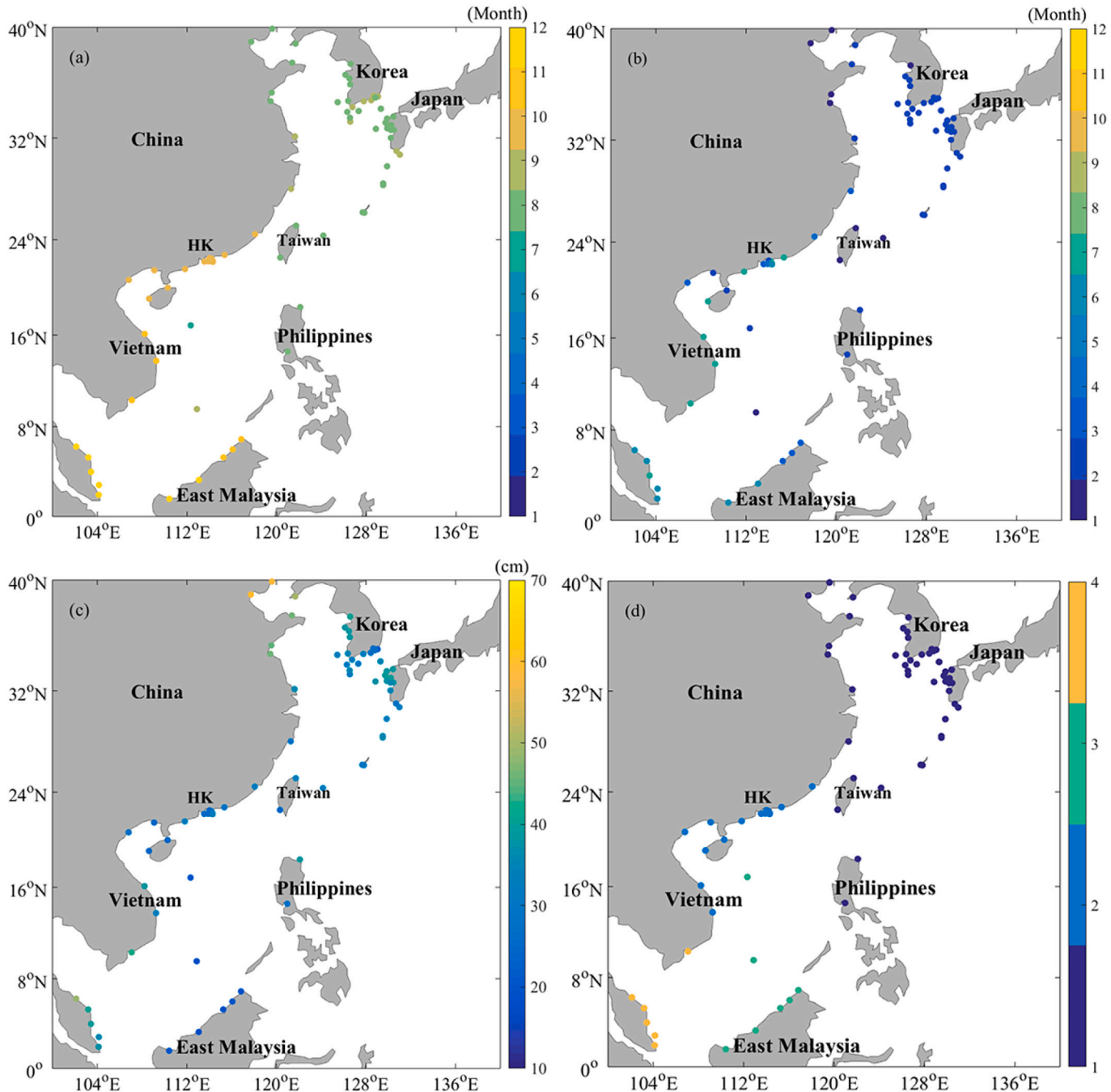

Fig. 4. The month of maximum (a), minimum (b) sea level, the annual range (c), and (d) four types of seasonal cycle (see text), for 81 tide gauge records over the maximum time span of each record during the NEMO-modelled period of 1959–2012.

extract the steric sea level as:

$$\Phi = h - \frac{p_b}{\rho_0 g} \qquad (5)$$

To explain variability of seasonal cycle in each tide gauge record, we a adopt multiple linear regression.

$$Y = \sum R_i X_i + K \qquad (6)$$

Where $X_{i(i=1,2,3)}$ are the time series of the three meteorological forcing factors: zonal (W_u) and meridional (W_v) wind stress, and sea level pressure (SLP), R_i denotes the regression coefficients of the X_i with Y, K is a constant, and Y is the sea level time series at a particular station. We used forcing factor time series from within the area of $\pm 4°$ around each tide gauge location. We selected the best performing of all possible combinations of forcing factors based on the F-statistic, with no prior assumptions about what meteorological forcing factors should be included (Moore et al., 2006, 2019). We then estimate the power of the leading forcing factors in explaining sea level as

$$S_i = R_i C_i \sigma X_i / \sigma Y \qquad (7)$$

Where $S_{i(i=1,2,3)}$ is the fractional contribution from each forcing to the total variance of the sea level, $\sigma X_{i(i=1,2,3)}$ denotes the standard deviation of X_i and σY denotes the standard deviation of the sea level time series. C_i denotes the correlation coefficients of the X_i with Y. The raw monthly and annual sea level curves and forcing factors for 4 archetypical stations are shown in Figs. S1 and S2.

The mixed layer depth (MLD) was calculated following Kara et al. (2000) using EN4.2.0 temperature and salinity data. We take temperature at 10 m depth as the reference and define the mixed layer as the depth at which the temperature change from the reference temperature is 1 °C.

4. Results

4.1. The seasonal sea level cycle from tide gauge records

The seasonal cycles for each of the 81 records are shown in Fig. S3. Fig. 4 summarizes the information on timing of maximum (Fig. 4a), minimum (Fig. 4b) sea level, and its annual range (Fig. 4c). To simplify the geographical distribution of the seasonality, we characterized the stations into four types, colour-coded in Fig. 4d. An archetype of each is shown in Fig. 5. Dalian (Fig. 5a) exemplifies the seasonal cycles of Type 1 stations in northern China and Taiwan, Korea, Japan as well as The Philippines. Maximum sea level occurs mostly in August and the minimum mostly in January. Type 2, exemplified by NPQB (Fig. 5b), have a seasonal sea-level with a relatively flat annual range, no obvious minimum between January to August, but a clearly defined peak in October. Type 3 stations have much less seasonality with no obvious maximum or minimum, for example Labuan II (Fig. 5c). The fourth type of seasonal cycle is a symmetric cosine cycle with a well-defined maximum and minimum. Geting in Gulf of Thailand (Fig. 5d) is an example of Type 4, with its peak in sea level in December and minimum in June.

The annual range of tide gauge records varies greatly across the 81 stations (shown in Table S3) from 18 to 59 cm. Qinhuangdao (No.3) and Tanggu (No.4) in the northern China have the largest ranges among all stations, while stations in East Malaysia have the smallest ranges which are all below 20 cm, the average range for all stations is 33 cm.

Inverse-barometer (IB) is primarily a static oceanic response to fluctuating atmospheric pressure loads (Wunsch and Stammer, 1997); a 1 mb increase of barometric pressure leads to a sea level fall of about 0.01 m. Table 1 shows the amplitude and phase of the annual and semi-annual harmonics at four typical stations before and after IB correction over the maximum time span within 1950–2012. The amplitude and phase of the annual and semi-annual harmonics from 81 observed tide gauge records are shown in Table S2. The harmonics are estimated from eq. 1. Type 1 station Dalian (No.1) has the amplitude of 24 cm before IB correction, and decreases to 15 cm after removing IB effects. Type 2 station NPQB has the amplitude of 11 cm before IB correction and increases to 15 cm after removing IB effects. Type 3 station Labuan II and Type 4 station Geting show slightly increase after IB correction.

The annual amplitudes present large variability on spatial scales before removing IB effects (shown in Table S2), Qinhuangdao (No.3) and Tanggu (No.4) in the Northern China have a maximum amplitude of 29 cm, Nansha (No.28) has a minimum amplitude of 6 cm, while the average amplitude across all records is 15 cm. The northern China and Taiwan, Korea, Japan and The Philippines have relatively higher
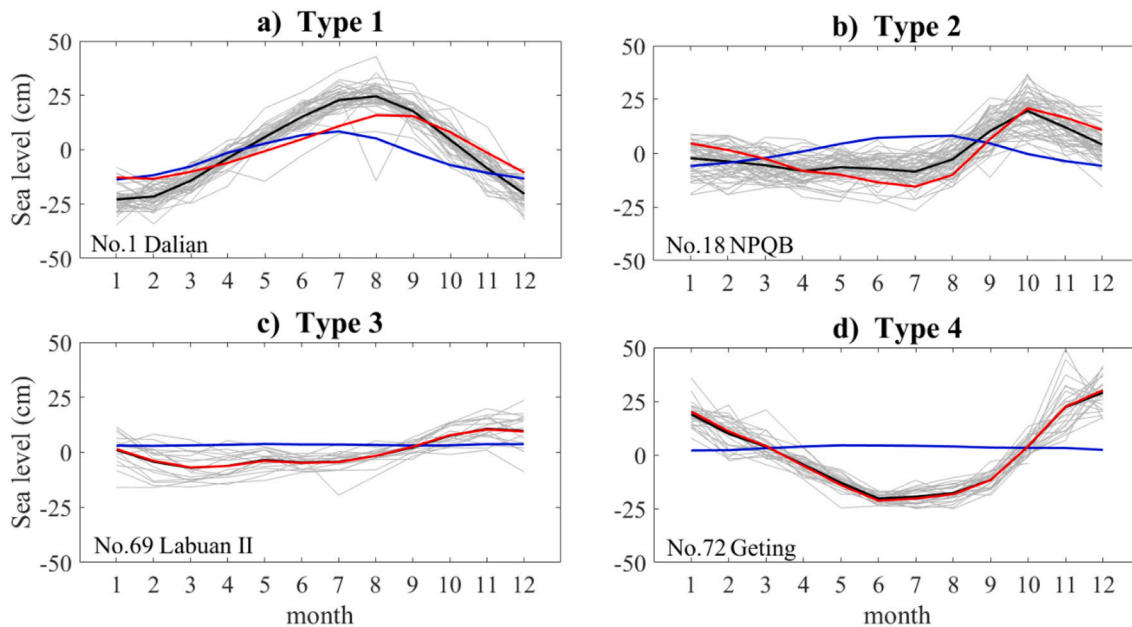

Fig. 5. Archetypes of the four modes of seasonal cycle. The gray lines are individual yearly records, and the thick black line is the averaged seasonal cycle. The blue line is the seasonal cycle of the inverse barometer (IB) correction. The red line is the seasonal cycle of sea level after removing IB effects. (For interpretation of the references to colour in this figure legend, the reader is referred to the web version of this article.)

Table 1

Seasonal harmonics from observed tide gauge record and IB corrected tide gauge records at the four archetypal stations (Nos. 1, 18, 69 and 72) over the maximum time span within 1959–2012. The uncertainty range is the 95% confidence interval for amplitude and phase. The variance explained refers to Eq. 1.

| | Observed tide gauge | | | | | IB corrected tide gauge | | | | |
| | Annual | | Semi-annual | | Explained Variance (%) | Annual | | Semi-annual | | Explained Variance (%) |
Type	Aa (cm)	Pa (days)	Asa (cm)	Psa (days)		Aa (cm)	Pa (days)	Asa (cm)	Psa (days)	
1	23.8 ± 0.7	194 ± 2	2.1 ± 0.7	32 ± 9	90	14.5 ± 0.7	212 ± 3	2.5 ± 0.7	40 ± 8	78
2	11.1 ± 0.8	289 ± 4	5.4 ± 0.8	75 ± 4	58	15.0 ± 0.8	317 ± 3	5.8 ± 0.8	78 ± 4	73
3	7.7 ± 1.1	298 ± 8	3.5 ± 1.1	109 ± 9	54	7.8 ± 1.0	298 ± 7	3.2 ± 1.0	108 ± 9	58
4	22.6 ± 0.9	349 ± 2	4.9 ± 0.9	117 ± 6	88	23.6 ± 0.9	349 ± 2	4.6 ± 0.9	119 ± 6	89

amplitude than the South China Sea with most values over 20 cm, with slightly lower amplitudes in the Gulf of Thailand. After correcting for IB effects, the changes of annual amplitudes due to IB correction varies from −11 to 5 cm across stations, the largest increase is from 11 to 16 cm at Tai Miu Wan in Hongkong (No.19) and Zhapo (No.23) while the largest decrease is from 29 to 17 or 18 cm at Qinhuangdao (No.3) and Tanggu (No.4) in northern China. For most stations in northern China and Taiwan, Korea, Japan and The Philippines, there are large decreases in the annual amplitude, which indicates that IB effects plays an important role in these areas. After correcting for IB effects, the highest annual amplitude is found in Geting (23.6), in the Gulf of Thailand. The phase of the annual cycle is typically delayed by the IB correction, and by up to 51 days at the Type 2 station Beihai (No.24), in the northern South China Sea. The changes of semi-annual amplitude caused by IB correction is much smaller compared with annual amplitude in most stations but still shows considerable differences, Zhapo (No.23) in the northern South China Sea presents the highest semi-annual amplitude of 7 cm.

Correcting for IB effects decreases the variance explained by the seasonal harmonics of eq. 1 by 3% ~ 30% (Table S2) for stations of Type 1, but increases variance accounted for at most stations of Type 2.

4.2. Atmospheric factors controlling the seasonal sea level cycle

We begin an exploration of the factors leading to the four types of seasonal cycle discussed earlier with the IB effects caused by pressure and the wind stress.

The monthly SLP (sea-level pressure) and average wind direction are

Table 2

Correlations between monthly mean sea level from tide gauge (TG), monthly SLP, monthly zonal (uwind) and meridional (vwind) winds.

	Type 1 (Dalian)	Type 2 (NPQB)	Type 3 (Labuan II)	Type 4 (Geting)
TG, SLP	−0.66	0.68	−0.50	0.77
TG, uwind	−0.79	−0.78	0.74	−0.92
TG, vwind	0.70	−0.85	−0.28	−0.96
SLP,uwind	0.64	−0.77	−0.45	−0.84
SLP, vwind	−0.82	−0.82	0.14*	−0.79
uwind, vwind	−0.79	0.77	−0.24	0.92

Correlations listed are the highest for the grid points within ±4° of the station.
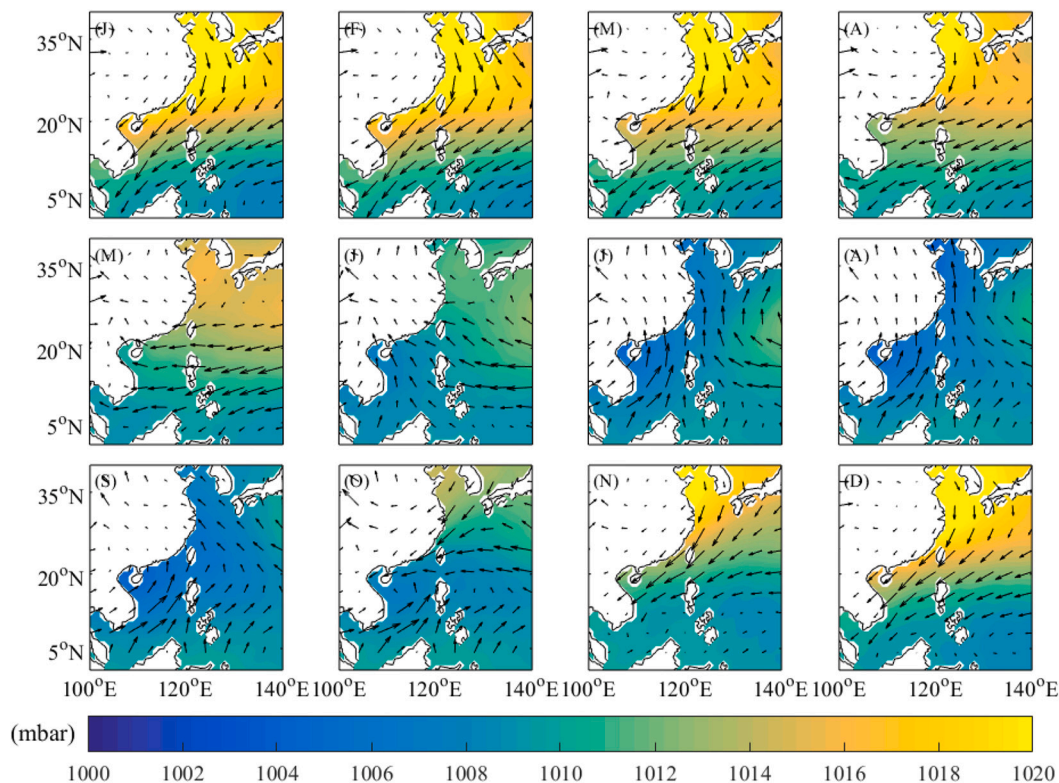* Correlation is not significant at the 95% level.

Fig. 6. The average monthly wind direction (arrows) and sea level pressure (colour bar) over 1959–2012. Each panel presents the months from January (J) to December (D).

shown in Fig. 6. Table 2 shows the correlation coefficients between different forcing factors. To quantitatively determine the contribution from atmospheric forcing factors, we plot the variance accounted for by the factors that best fit the multiple linear regression model (Eq. 6) in Fig. 7. Fig. 7a is the variance explained at each tide gauge site by atmospheric forcing factors before removing IB effects, and Fig. 7b is after doing the IB correction. Fig.6 shows the monthly wind direction and SLP in our study area which then use to better consider physical mechanisms that drive seasonal variations. The correlation coefficients between tide gauge record and different meteorological forcing factors (Table 2), and the variances explained by each forcing (Fig.7) help identify the influences of atmospheric factors on seasonal sea level variability.

For most stations of Type 1 which are in northern China and Taiwan, Korea, Japan and The Philippines, SLP is the main contributor before removing the IB effects as SLP best fits the multiple linear regression model. The IB correction produces changes in the seasonal amplitude from a reduction of 11 cm to an increase of 5 cm across stations, with greatest influence on Types 1 and 2. Table 2 shows that the monthly tide gauge record in Dalian is anti-correlated with SLP ($r = -0.66$) and zonal wind ($r = -0.79$) but correlated with meridional wind ($r = 0.70$). From Fig. 7 we see that before correcting IB effects, SLP is the main contributor to the sea level variability in Dalian while after IB correction, zonal wind contributes the largest. The annual peak at Dalian between July and August is due to the IB effects caused by low atmospheric pressure in summer (Fig. 6). Similarly, for most stations in northern China and Taiwan, Korea, Japan and The Philippines, the IB correction makes large reductions in the annual amplitude, consistent with the study of Feng

et al. (2015). After the IB correction, total explained variance of tide gauge records decreases - by up to 43% in Kaohsiung II.

Sea level at NPQB (Type 2) is correlated with surrounding SLP (0.68) but anti-correlated with both zonal (-0.78) and meridional (-0.85) winds. SLP works in a different way from Dalian, with strong anti-correlation between SLP and meridional wind ($r = -0.82$) as well as zonal wind ($r = -0.77$) hence we infer that SLP field primarily influences the sea level variability associated with wind stress rather than IB effects.

For most stations of Type 3 and Type 4 located in Vietnam and Malaysia, zonal wind or meridional wind are the best predictors. Labuan II (Type 3) is much less correlated with meridional wind ($r = -0.28$), than are the other 3 types. It is better correlated with SLP ($r = -0.50$) and zonal wind ($r = 0.74$). Zonal wind is the main atmospheric contributor to the sea level variability in Labuan II as it best fits the linear regression.

At Geting (Type 4) SLP is well correlated with sea level ($r = 0.77$), both sea level and SLP are high in winter and low in summer, but both zonal wind ($r = -0.92$) and meridional wind ($r = -0.96$) are even better anti-correlated with it. Meridional wind best fits the linear regression model, indicating that wind is the main forcing factor suggesting that SLP field influences the sea level variability associated with wind stress. This is explained by the strong association between the monsoon and a distinctive North to South dipole anomaly in the SLP field (Fig. 6). The Northeast Monsoon pushes water masses from the South China Sea towards the Gulf of Thailand in winter while the Southwest Monsoon drives them away in summer. The Southwest Monsoon also pushes water
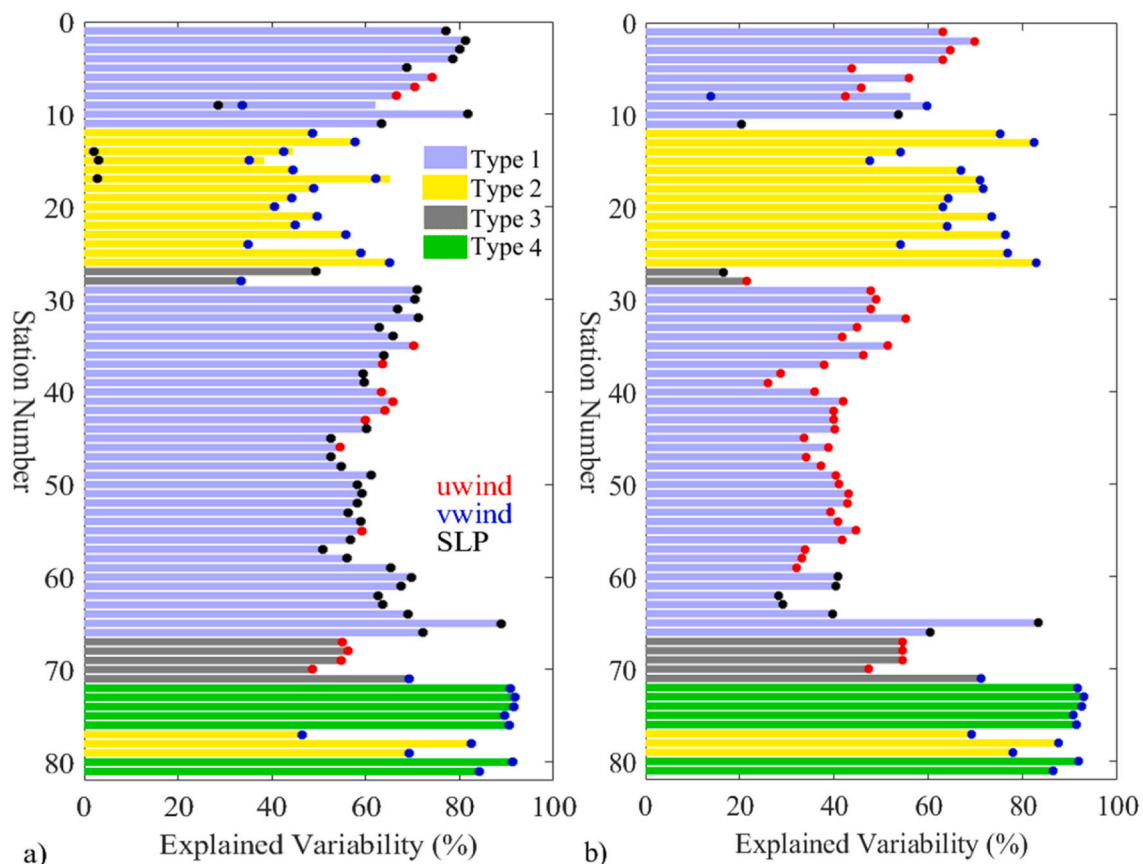

Fig. 7. Total explained variance (abscissa, length of bar) for each tide gauge station (ordinate) from the best fit multiple linear regression model (Eq. 6) of monthly sea level record as a function of meteorological forcing factors. Panel is (a) before and (b) after IB correction. The data span the maximum interval of each station record between 1959 and 2012. The colour of the bars represents the 4 different station types: Type 1 (blue), type 2 (yellow) type 3 (gray) and type 4 (green). The dots in each bar show the variance accounted for each station by each of the 3 forcing factors in Eq. 6 (red: zonal wind, blue: meridional wind, black: SLP), with the total variance explained as the sum of the 3 given by the length of each bar. For most stations a single forcing factor in Eq. 6 produces the best model F-Statistic. (For interpretation of the references to colour in this figure legend, the reader is referred to the web version of this article.)

mass towards Dalian in summer which contributes to its summer peak (Saramul and Ezer, 2014; Feng et al., 2015; Mohan and Vethamony, 2017).

Quantitatively estimation of the contribution from atmospheric forcing factors before and after the IB correction (Fig. 7) shows that for many stations of Type 1, SLP is the main contributor. After the IB correction the total explained variance of tide gauge records decreases, by up to 43% in Kaohsiung II (Fig. 7), therefore we conclude SLP mainly influences the seasonal variability through IB effects. For most stations of Type 2, Type 3 and Type 4, zonal wind or meridional wind are the best predictors (Fig. 7). For most stations in the South China Sea, the total explained variance of tide gauge record increases after IB correction (Fig. 7).

.

4.3. Analysis of sea surface height from satellite altimetry and the NEMO model

We spatially extend the tide gauge information using sea surface height anomalies from IB corrected satellite altimetry data (AVISO with Dynamic Atmospheric Correction). The amplitude and phase of annual harmonics of sea surface height anomalies from satellite altimetry and NEMO Sea Surface Height (SSH) are shown in Fig. 8. The annual amplitudes are much smaller in the deep ocean (<10 cm) than for coastal regions. The spatial variability of the annual amplitude and phase from altimetry are generally coherent with NEMO SSH. But NEMO model outputs provide about ten times higher resolution and better spatial coverage than the satellite altimetry, especially along the coast. From Fig.8, the South China Sea has higher annual amplitudes than in the northern and eastern Chinese coasts where the annual amplitudes range from 6 to 15 cm; the Gulf of Thailand has the highest annual amplitude (18–24 cm). The annual harmonic at the Chinese coast, Japan and Korea peak between July and October while the South China Sea and the Gulf of Thailand peak in November and December.

The semi-annual harmonic (Fig. S4) varies less than the annual harmonic, although there is a considerable difference in amplitude between the northern coasts and the South China Sea. The highest amplitude of the semi-annual (6 cm) is not in the Gulf of Thailand but along the coast of northern South China Sea. Again, the deep ocean has smaller amplitudes than the coast, but in contrast with the annual harmonic, the semi-annual peaks later in the open ocean than on the continental shelf.
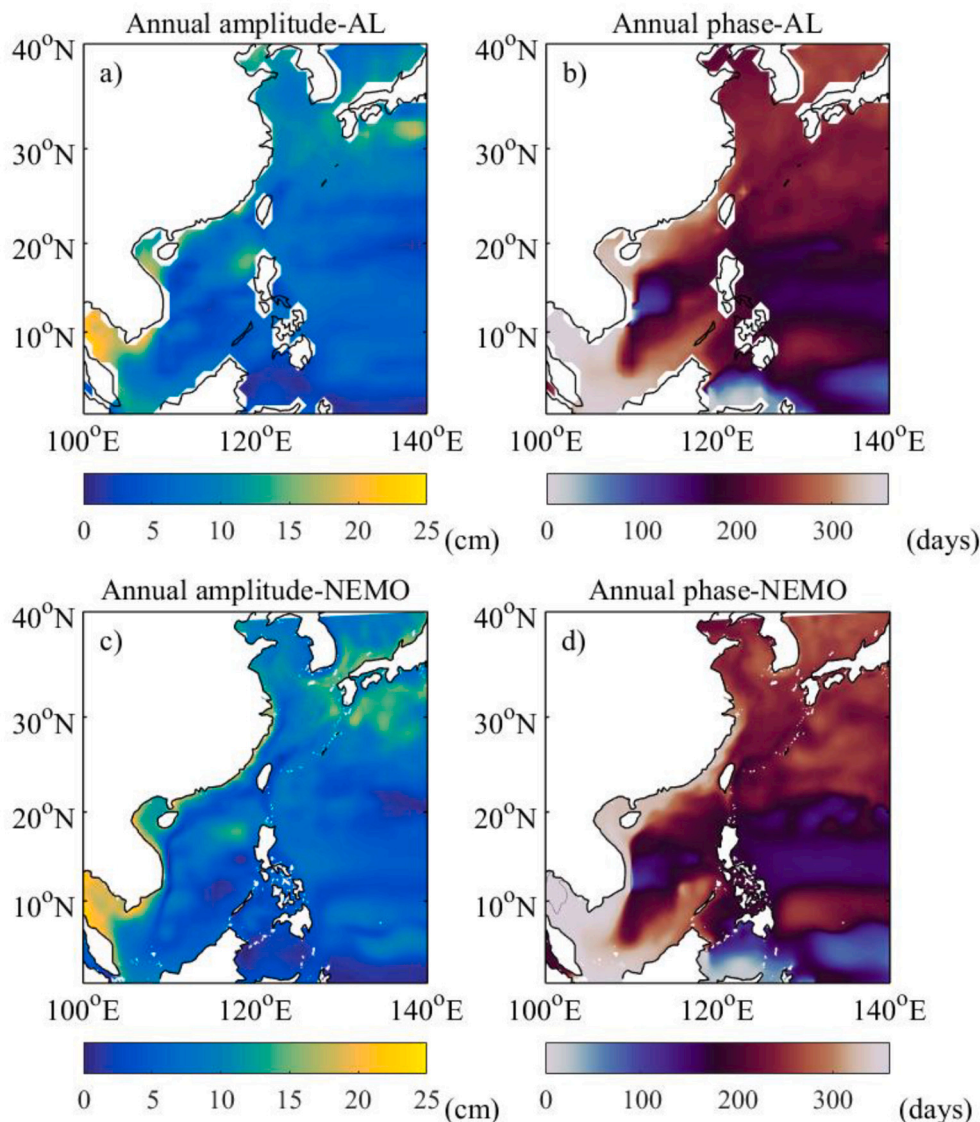

Fig. 8. Seasonal harmonics from the (a, b) satellite altimetry and (c, d) NEMO SSH over 1993–2012. Amplitude (cm) and phase (days) of annual sea level cycle. The linear trend has been removed.

To compare the seasonal sea level cycle along the coast from different sources of data, we calculate the annual amplitude and phase of the seasonal harmonics from IB corrected tide gauge records, satellite altimetry and NEMO SSH at all stations over 1993–2012 period; the results are shown in Fig.9. There are differences in the annual amplitude and phase from the three sources. For most stations, satellite altimetry and NEMO SSH underestimate the amplitude of the annual cycle along the coast, by up to 12 cm for satellite altimetry and 7 cm for NEMO. Altimetry and NEMO lead tide gauge records in many stations, by up to 42 days for altimetry and 46 days for NEMO. For stations outside Korea, the annual amplitude of NEMO is closer to the IB corrected tide gauge records than satellite altimetry. Hence NEMO generally performs well in simulating the sea level variability along the Chinese coast except for some stations in northern China, Korea, and Japan. The differences in annual harmonics of the sea level between satellite altimetry, NEMO and tide gauge records are mainly due to coarse resolution and lack of representation of physical mechanisms near the coast, such as coastal currents (Amiruddin et al., 2015).

The total sea level is the sum of three contributors: the barometric term, the steric term, and the contribution from ocean bottom pressure. The steric sea level change caused by the thermal expansion of seawater is an important contributor to the seasonal sea level variability. Ocean bottom pressure measures the barotropic variations which gives insight into changes in ocean circulation (Köhl et al., 2012; Johnson and Chambers, 2013). We have analyzed the general spatial characteristics of the seasonal cycle around the China seas, now we focus on the steric component and ocean bottom pressure. There are only sparse observations of temperature and salinity data below 2000 m depth, but steric sea level can also be calculated by the difference between sea surface height and sea level changes caused by ocean bottom pressure from NEMO model outputs. Fig.10 presents the average monthly tide gauge record after IB correction, steric sea level calculated with the combination of observational temperature and salinity data, NEMO steric sea level and sea level change caused by ocean bottom pressure from NEMO model outputs at the four archetypical stations.

At Dalian (Type 1), NEMO steric sea level amplitude is twice that observed from the station. The sea level change inferred by bottom pressure peaks in September with amplitude of 3.9 cm, about half the steric sea level change. Thus, steric effects are dominant in Dalian.

In contrast at NPQB (Type 2), the seasonal steric cycle is quite different from sea level. Ocean bottom pressure has much larger seasonal variability and it is the main contributor to seasonal sea level cycle. For Labuan II (Type 3) and Geting (Type 4), ocean bottom pressure is also be the main contributor to seasonal sea level variability and has similar seasonal cycle as the tide gauge record. Geting (Type 4) is in the Gulf of Thailand, which is dominated by a barotropic response and freshwater exchange driven by the monsoon.

To gain a better understanding of the spatial variations of steric sea level over our study area, we calculated the average steric sea level from the NEMO model (Fig. 11). Steric sea level has bigger seasonal variability in the deep ocean than the continental shelves. Steric sea levels are higher in summer than winter due to thermal expansion, with the largest amplitudes north of 20°N.

Wind can influence the sea level change through both barotropic and baroclinic response. The baroclinic response to wind also affects the seasonality of steric component. Wind field can drive the changes in thermocline through Ekman pumping which can influence the seasonal variability of steric sea level. In this mechanism, the three-dimensional circulation of sea water is affected through wind stress curl. Fig. 12 shows the monthly average wind stress curl around the China Seas while Fig. 13 shows the monthly average mixed layer depth. Wind stress curl displays obvious seasonal variations. In the winter half year, the Chinese coast and the west side of the South China Sea have negative curl, and the center of the negative curl is near the shore of the South China Sea, which causes the mixed layer depth to thicken, and the thermocline depth to fall, so the steric sea level rises; While the east side of the South China Sea exhibits positive curl which causes the mixed layer depth to thin, the thermocline to rise, and steric sea level to decrease. In summer, the cyclonic wind field driven by positive wind stress curl expands eastward and compresses the anticyclonic wind field closer to the
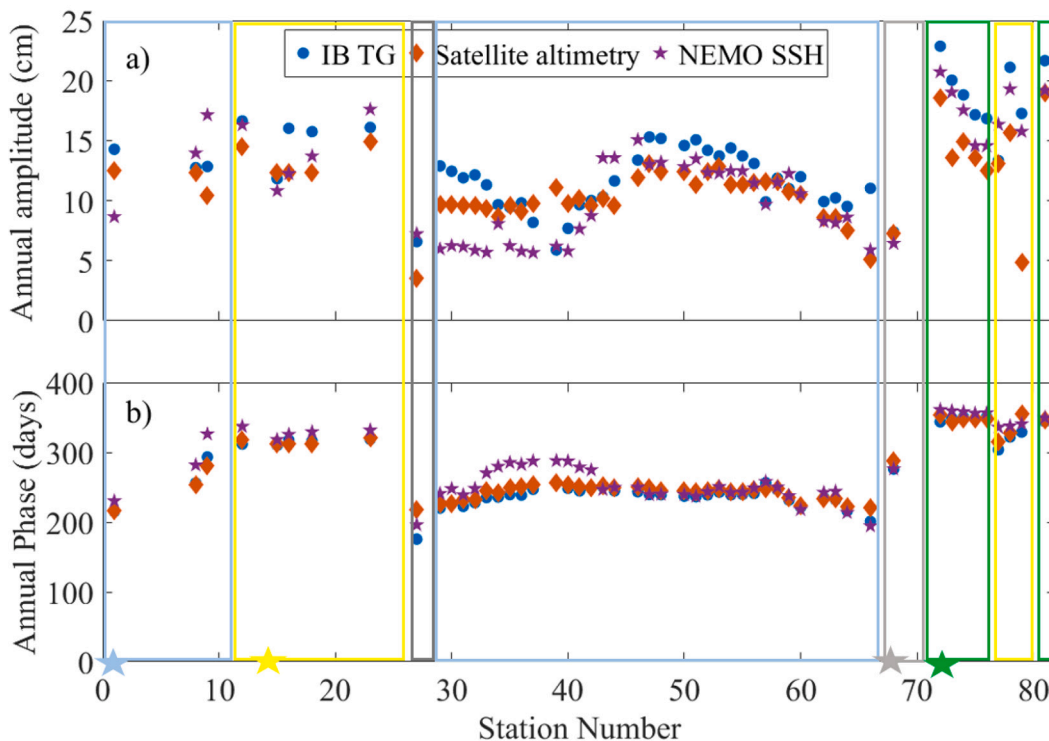

Fig. 9. The annual seasonal harmonics for IB-corrected tide gauge stations, satellite altimetry and NEMO model outputs over 1993–2012. The linear trend has been removed. Large coloured stars on the abscissa and boxed regions delimit station type as in Fig. 7.
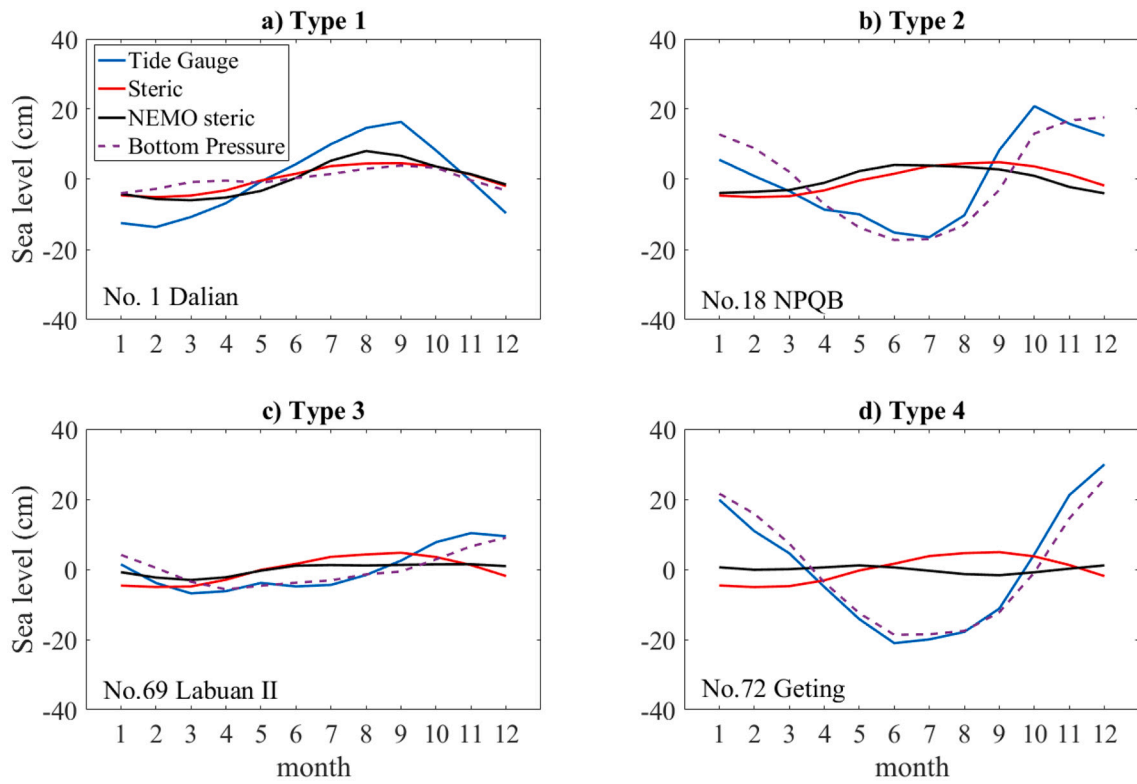
Fig. 10. The average monthly tide gauge record after correcting for IB effects, steric sea level calculated from observational data, NEMO steric sea level and sea level change caused by ocean bottom pressure from NEMO at the four representative stations over 1993–2012.
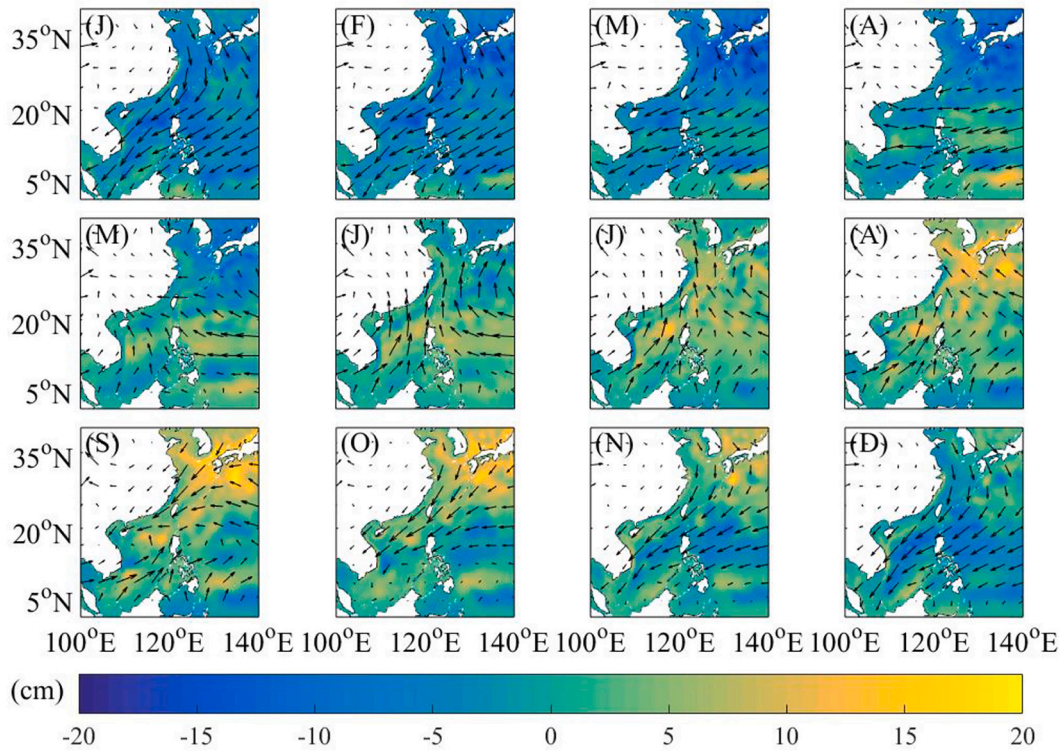

Fig. 11. The average monthly NEMO steric sea level during 1993–2012 (Units: cm). The arrows indicate the wind direction.
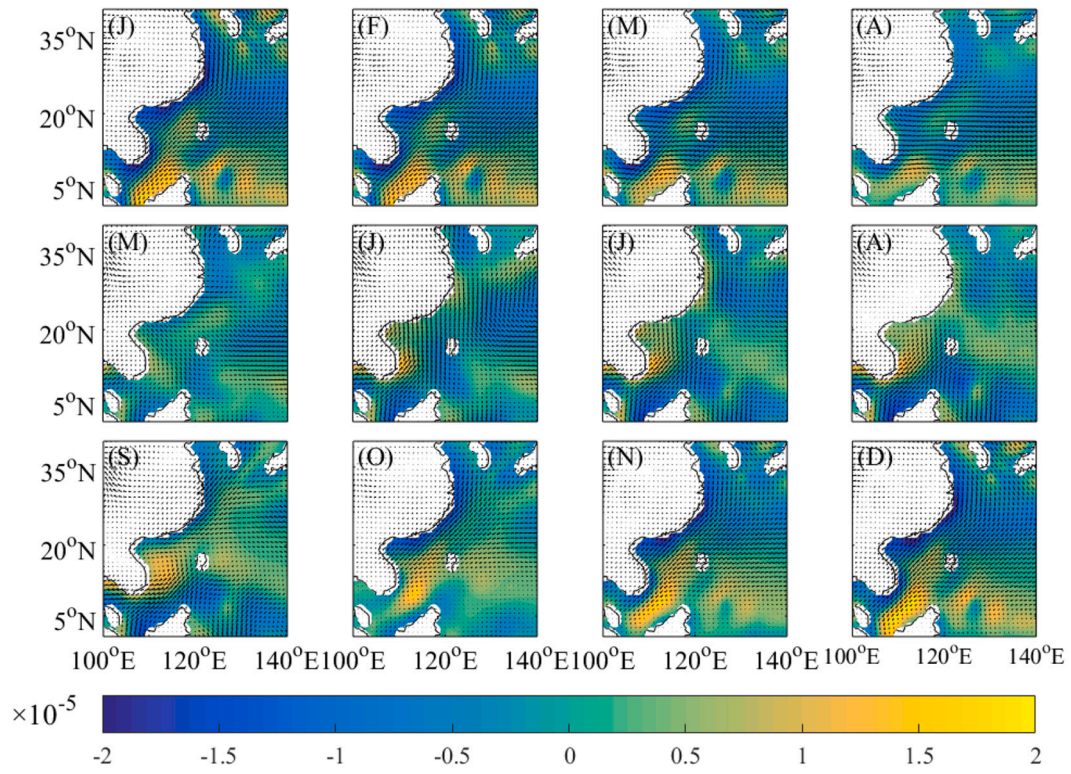
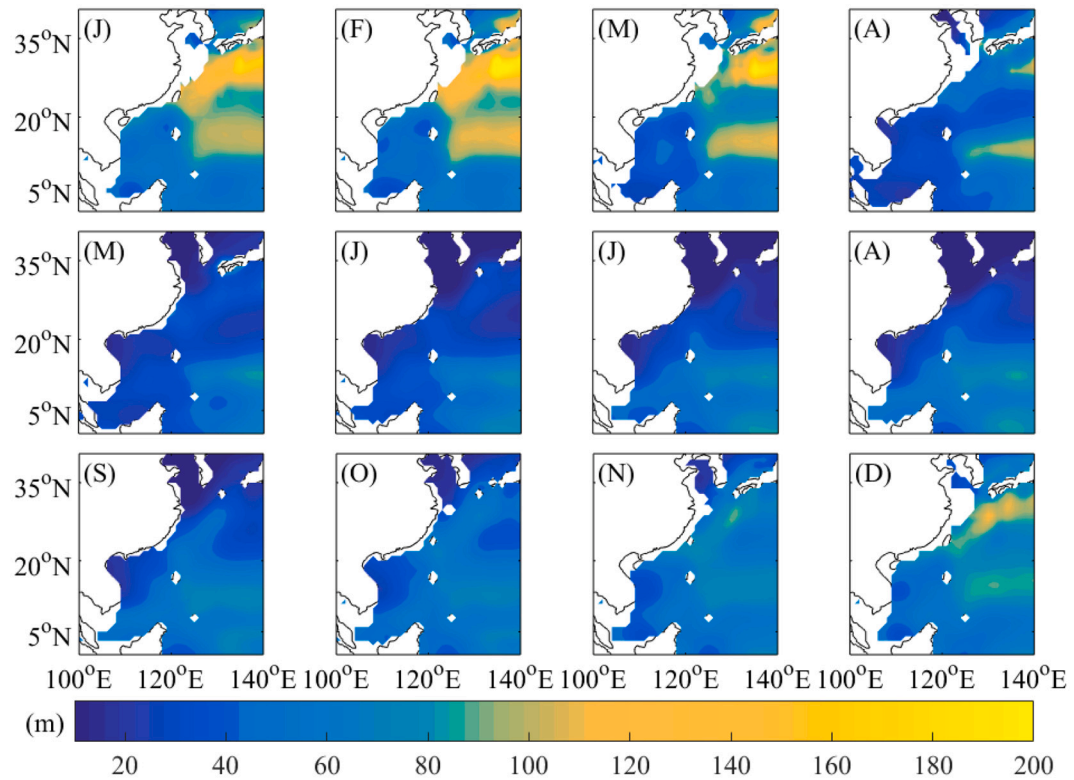**Fig. 12.** The average monthly wind stress curl over 1993–2012 (Units: s^{-1}).

Fig. 13. The average monthly mixed layer depth over 1993–2012 (Units: m).

eastern side. These differences in the thermocline depths help to form the southward western boundary current in winter.

5. Discussion

Feng et al. (2015) investigated the seasonal sea level variability in the northwest Pacific using tide gauge records and AVISO satellite altimetry, they classify the 120 tide gauges into six subregions according to their geographical location and explore the seasonal variability in the study area, they found that over their whole study area, IB effects had significant influences on the annual cycle with the largest amplitude of 12 cm in the East China Sea (comprising northern and eastern China coasts), which is consistent with our study as we have the largest decrease of annual amplitude in Qinhuangdao and Tanggu by 11 cm after IB correction. In their study, contribution from ocean bottom pressure were calculated as the residual after removing IB effects and steric components from the total sea level, results revealed that wind stress and surface currents play significant role in the marginal seas and the tropics which are also consistent with our study. However, and different from Feng et al., we divide all tide gauge stations into groups based on both geographical location and the characteristics of mean seasonal cycle. Then just four groups are sufficient to characterize all the tide gauge station behaviour in the region. Type 1 stations in northern China and Taiwan, Korea, Japan and The Philippines have an asymmetric sinusoid with maximum sea level mostly occurring in August and the minimum mostly in January; Type 2 stations located along the eastern and southern Chinese coasts have a clearly defined peak in October on a flat background with no obvious minimum between January to August; Type 3 stations in East Malaysia have a relatively flat signal; Type 4 stations in Vietnam and the Gulf of Thailand present a symmetric co-sinusoid signal with peak sea level in December and minimum in June. While the defining characteristics of the group are somewhat of a subjective choice, they illustrate different features of mean seasonal sea level cycle attributable to different meteorological forcing factors. They are also grouped geographically which implies commonality in some seasonal meteorological characteristics. The self-consistent nature of the grouping with dominant forcing factors and geography supports our contention that the grouping has value.

Generally, NEMO is good at simulating the seasonal variability around the China Seas especially in the southern areas, however in the northern areas, NEMO is underestimating the seasonal variability more than satellite altimetry. The physical mechanism of the underestimation from NEMO in the northern region remains unknown and is a topic for future work.

Sparsely distributed tide gauge records and the relatively short time span of satellite altimetry data limit our understanding of the seasonal sea level cycle on coastal regions, thus seasonal variations are usually not included in the future sea level projection. In this paper we made use of 81 tide gauge records along with satellite altimetry and high-resolution NEMO model outputs including sea surface height and ocean bottom pressure, dividing all stations into four types and then exploring the main drivers for the seasonal variability at each archetypal station. The attribution of driving factor made use of a novel multiple linear regression procedure (Eq. 6) and which usually isolates a single meteorological factor as the dominant controller of seasonality. This controller we find is consistent with the geographic spread of stations, and features of the regional SLP and wind field. This kind of analysis is intrinsically linear whereas we may expect atmospheric forcing to interact in rather non-linear ways especially considering the non-stationary climate. Hence a possible improvement may come from using a wider spectrum of model drivers and an Akaike or Baysian information criterion as a model selecting method.

Comparison with the tide gauge records shows that despite the underestimation of amplitude from the NEMO model outputs, generally NEMO is good at simulating the seasonal variability around the South China Seas. Hence further efforts should be made to improve the NEMO

simulation, then it can be used to quantitatively determine the contributions of different components to seasonal variability, making the seasonal variability included in the future sea level projection possible.

6. Conclusions

Previous studies on the seasonal cycle and variability around the China Seas mainly focused on the South China Sea, made use of tide gauge records, satellite altimetry as well as steric sea level to analyze the sea level change characteristics systematically. In this paper, we also introduce high-resolution model outputs of sea surface height and ocean bottom pressure from NEMO, into the analysis of seasonal sea level cycle and variability. We make use of exemplifying stations to represent four broader regions, discuss the spatial and temporal variations of seasonal sea level cycle and the physical mechanism.

The months of maximum, minimum, and annual range of the seasonal cycle in 81 tide gauge records in the study area all show obvious spatial differences. To quantitatively analyze the seasonal cycles of all stations, and the contribution of IB correction, we calculate the amplitude and phase of annual and semi-annual cycles of all tide gauge records before and after removing IB effects. The results show that IB correction reduces the annual amplitude of most stations in the northern China and Taiwan, Korea, Japan and The Philippines, among which the largest decreases are in Qinhuangdao and Tanggu in the northern China, where the annual amplitude decreased by 11 cm. After correction, the highest amplitude is in the Gulf of Thailand. For the northern China and Taiwan, Korea, Japan and The Philippines, IB correction results in significant reduction of variance explained by seasonal harmonics, while for most stations in the South China Sea, Malaysia and Vietnam, the explained variance increases after IB correction.

Dalian (Type 1), NPQB (Type 2), Labuan II (Type 3) and Geting (Type 4) were taken as four archetypal stations to determine the main drivers for the seasonal variability: Type 1 has an asymmetric sinusoidal cycle; Type 2 has a clearly defined peak on a flat background; Type 3 has a relatively flat signal; Type 4 has a symmetric co-sinusoidal cycle. We analyze the correlation between tide gauge record and three meteorological forcing factors include sea level pressure, zonal wind and meridional wind at each typical station respectively, fit the tide gauge record and all meteorological forcing factors using multivariate linear regression analysis. The results show that sea level pressure is the main contributing factor for most stations of Type 1. While for most stations of Type 2, Type 3 and Type 4, the main contributor is zonal wind and meridional wind.

To understand the seasonal variability over the whole study area, we also used AVISO satellite altimetry combined with NEMO model outputs. In coastal continental shelves, the annual amplitude are larger than in the deep ocean. Annual amplitude peaks between July and October off the coast of China, Japan and South Korea, and in November and December in the South China Sea and the Gulf of Thailand. The annual amplitude of deep ocean reaches its peak earlier than the coastal continental shelves, between June and September. The spatial differences of semi-annual harmonics are small but still obvious. The maximum amplitude of the semi-annual harmonic is 6 cm found in the north of the South China Sea.

We also analyzed the contribution of NEMO steric sea level, steric sea level with observational temperature and salinity data, sea surface height and sea level change caused by ocean bottom pressure from NEMO at the four representative stations. The results show that after IB correction, steric is the most important contributor to seasonal sea level cycle in Dalian (Type 1), while for NPQB (Type 2), Labuan II (Type 3) and Geting (Type 4), ocean bottom pressure associated with wind and ocean circulation contributes much more than other factors.

Declaration of Competing Interest

The authors declare that they have no known competing financial

interests or personal relationships that could have appeared to influence the work reported in this paper.

Appendix A. Supplementary data

Supplementary data to this article can be found online at https://doi.org/10.1016/j.gloplacha.2022.103819.

References

Abadie, L.M., Jackson, L.P., Murieta, E.S.D., Jevrejeva, S., Galarraga, I., 2020. Comparing urban coastal flood risk in 136 cities under two alternative sea-level projections: RCP 8.5 and an expert opinion-based high-end scenario. https://doi.org/10.1016/j.ocecoaman.2020.105249.

Amiruddin, A.M., Haigh, I.D., Tsimplis, M.N., et al., 2015. The seasonal cycle and variability of sea level in the South China Sea. Geophysical Res. Oceans 120, 5490–5513. https://doi.org/10.1002/2015JC010923.

Brodeau, L., Barnier, B., Treguier, A.M., Penduff, T., Gulev, S., 2010. An ERA40-based atmospheric forcing for global ocean circulation models. Ocean Model 31, 88–104. https://doi.org/10.1016/j.ocemod.2009.10.005.

Carrère, L., Lyard, F., 2003. Modeling the barotropic response of the global ocean to atmospheric wind and pressure forcing: comparisons with observations. Geophys. Res. Lett. 30 (6), 1275. https://doi.org/10.1029/2002GL016473.

Cheng, X., Qi, Y., 2010. On steric and mass-induced contributions to the annual sea-level variations in the South China Sea. Glob. Planet. Chang. 72 (3), 227–233. https://doi.org/10.1016/j.gloplacha.2010.05.002.

Compo, G.P., et al., 2011. The twentieth century reanalysis project. Q. J. R. Meteorol. Soc. 137 (654), 1–28. https://doi.org/10.1002/qj.776.

Dangendorf, S., et al., 2012. Mean sea level variability and influence of the North Atlantic Oscillation on long-term trends in the German Bight. Water 4 (1), 170–195. https://doi.org/10.3390/w4010170.

Dangendorf, S., Mudersbach, C., Wahl, T., Jensen, J., 2013. Characteristics of intra-, inter-annual and decadal sea-level variability and the role of meteorological forcing: the long record of Cuxhaven. Ocean Dyn. 63 (2–3), 209–224. https://doi.org/10.1007/s10236-013-0598-0.

Dangendorf, S., Calafat, F.M., Arns, A., Wahl, T., Haigh, I.D., Jensen, J., 2014. Mean sea level variability in the North Sea: Processes and implications. J. Geophys. Res. Oceans. 2, 1022–1037. https://doi.org/10.1002/2013JC009415.

Ding, X., Zheng, D., Chen, Y., Chao, J., Li, Z., 2001. Sea level change in Hong Kong from tide gauge measurements of 1954-1999. J. Geod. 74, 683–689. https://doi.org/10.1007/s001900000128.

Dussin, R., Barnier, B., Brodeau, L., 2014. The Making of Drakkar Forcing Set DFS5. DRAKKAR/MyOcean Rep. 05-10-14, LGGE, Grenoble, France.

Feng, X., Tsimplis, M.N., Marcos, M., Calafat, F.M., Zheng, J., Jordà, G., Cipollini, P., 2015. Spatial and temporal variations of the seasonal sea level cycle in the Northwest Pacific. J Geophys Res: Oceans 120, 7091–7112. https://doi.org/10.1002/2015JC011154.

Gill, A.E., Niiler, P.P., 1973. The theory of the seasonal variability in the ocean. Deep-Sea Res. Oceanogr. Abstr. 20 (2), 141–177. https://doi.org/10.1016/0011-7471(73)90049-1.

Good, S.A., Martin, M.J., Rayner, N.A., 2013. EN4: quality controlled ocean temperature and salinity profiles and monthly objective analyses with uncertainty estimates. J. Geophys. Res. Oceans. 118, 6704–6716. https://doi.org/10.1002/2013JC009067.

Gouretski, V., Reseghetti, F., 2010. On depth and temperature biases in bathythermograph data: development of a new correction scheme based on analysis of a global ocean database. Deep-Sea Rese. I. 57, 6. https://doi.org/10.1016/j.dsr.2010.03.011.

Holgate, S.J., Matthews, A., Woodworth, P.L., Rickards, L.J., Tamisiea, M.E., Bradshaw, E., Foden, P.R., Gordon, K.M., Jevrejeva, S., Pugh, J., 2013. New data systems and products at the permanent service for mean sea level. J. Coast. Res. 29 (3), 493–504. https://doi.org/10.2112/JCOASTRES-D-12-00175.1.

Hughes, Chris W., Williams, Joanne, Blaker, Adam, Coward, Andrew, Stepanov, Vladimir, 2018. A window on the deep ocean: the special value of ocean bottom pressure for monitoring the large-scale, deep-ocean circulation. Prog. Oceanogr. 161, 19–46. https://doi.org/10.1016/j.pocean.2018.01.011.

Jevrejeva, S., Jackson, L.P., Grinsted, A., Riva, R., Moore, J.C., 2016. Coastal Sea-level rise with warming above 2 degree. Proc. Natl. Acad. Sci. https://doi.org/10.1073/pnas.1605312113.

Jevrejeva, S., Frederikse, T., Kopp, R.E., Cozannet, G.Le., Jackson, L.P., van de Wal, R.S. W., 2019. Probabilistic sea level projections at the coast by 2100. Surv. Geophys. 40, 1673–1696. https://doi.org/10.1007/s10712-019-09550-y.

Johnson, G.C., Chambers, D.P., 2013. Ocean bottom pressure seasonal cycles and decadal trends from GRACE. Release-05: Ocean circulation implications. J. Geophys. Res. Oceans 118, 4228–4240. https://doi.org/10.1002/jgrc.20307.

Kalnay, et al., 1996. The NCEP/NCAR 40-year reanalysis project. Bull. Amer. Meteor. Soc. 77, 437–470.

Kara, A.B., Rochford, P.A., Hurlburt, H.E., 2000. An optimal definition for ocean mixed layer depth. J. Geophys. Res. 16, 803–821. https://doi.org/10.1029/2000JC900072.

Köhl, A., Siegismund, F., Stammer, D., 2012. Impact of assimilating bottom pressure anomalies from GRACE on ocean circulation estimates. J. Geophys. Res. 117, C04032. https://doi.org/10.1029/2011JC007623.

Marsh, R., de Cuevas, B.A., Coward, A.C., Jacquin, J., Hirschi, J.J.M., Aksenov, Y., Nurser, A.J.G., Josey, S.A., 2009. Recent changes in the North Atlantic circulation simulated with eddy-permitting and eddy-resolving ocean models. Ocean Model 28, 226–239. https://doi.org/10.1016/j.ocemod.2009.02.007.

McDougall, T.J., Barker, P.M., 2011. Getting started with TEOS-10 and the Gibbs Seawater (GSW) Oceanographic Toolbox. SCOR/IAPSO WG 127, 1–28.

Menendez, M., Mendez, F.J., Losada, I., 2009. Forecasting seasonal to interannual variability in extreme sea levels. ICES J. Mar. Sci. 66 (7), 1490–1496. https://doi.org/10.1093/icesjms/fsp095.

Moat, B.I., Josey, S.A., Sinha, B., Blaker, A.T., Smeed, D.A., McCarthy, G.D., Johns, W.E., Hirschi, J.J.-M., Frajka-Williams, E., Rayner, D., Duchez, A., Coward, A.C., 2016. Major variations in subtropical North Atlantic heat transport at short (5 day) time-scales and their causes. J. Geophys. Res. (Oceans) 121, 3237–3249. https://doi.org/10.1002/2016JC011660.

Mohan, S., Vethamony, P., 2017. Interannual and long-term sea level variability in the eastern Indian Ocean and South China Sea. Clim. Dyn. 50 (9), 3195–3217. https://doi.org/10.1007/s00382-017-3800-0.

Moore, J.C., Kekonen, T., Grinsted, A., Isaksson, E., 2006. Sulfate source inventories from a Svalbard ice core record spanning the Industrial Revolution. J. Geophys. Res. 111, D15307. https://doi.org/10.1029/2005JD006453.

Moore, J.C., Yue, C., Zhao, L., Guo, X., Watanabe, S., Ji, D., 2019. Greenland ice sheet response to stratospheric aerosol injection geoengineering. Earth's Future 7. https://doi.org/10.1029/2019EF001393.

Permanent Service for Mean Sea level (PSMSL), 2017. Tide Gauge Data. Retrieved 09 Oct 2017 from. http://www.psmsl.org/data/obtaining/.

Pugh, D., Woodworth, P., 2014. Sea-Level Science: Understanding Tides, Surges, Tsunamis and Mean Sea-Level Changes. Cambridge Univ. Press, Cambridge, U. K.

Qu, Y., Jevrejeva, S., Jackson, L.P., Moore, J.C., 2019. Coastal Sea level rise around the China Seas. Glob. Planet. Chang. 172, 454–463. https://doi.org/10.1016/j.gloplacha.2018.11.005.

Saramul, S., Ezer, T., 2014. Spatial variations of sea level along the coast of Thailand: Impacts of extreme land subsidence, earthquakes and the seasonal monsoon. Glob. Planet. Chang. 122, 70–81. https://doi.org/10.1016/j.gloplacha.2014.08.012.

Tsimplis, M.N., Woodworth, P.L., 1994. The global distribution of the seasonal sea level cycle calculated from coastal tide gauge data. J. Geophys. Res. 99 (C8) https://doi.org/10.1029/94JC01115, 16,031–16,039.

Vinogradov, S.V., Ponte, R.M., Heimbach, P., Wunsch, C., 2008. The mean seasonal cycle in sea level estimated from a data-constrained general circulation model. J. Geophys. Re. 113, C03032. https://doi.org/10.1029/2007JC004496.

Wahl, T., Calafat, F.M., Luther, M.E., 2014. Rapid changes in the seasonal sea level cycle along the US Gulf coast from the late 20th cen- tury. Geophys. Res. Lett. 41, 491–498. https://doi.org/10.1002/2013GL058777.

Woodruff, J.D., Irish, J.L., Camargo, S.J., 2013. Coastal flooding by tropical cyclones and sea level rise. Nature 504 (7478), 44–52.

Wunsch, C., Stammer, D., 1997. Atmospheric loading and the oceanic "Inverted Barometer" effect. Rev. Geophys. 35 (1), 79–107. https://doi.org/10.1029/96RG03037.